



# Acoustic streaming near a sharp structure and its mixing performance characterization

Chuanyu Zhang<sup>1</sup> · Xiaofeng Guo<sup>1,3</sup> · Philippe Brunet<sup>2</sup> · Maxime Costalonga<sup>4</sup> · Laurent Royon<sup>1,2</sup>

Received: 27 April 2019 / Accepted: 25 July 2019  
© Springer-Verlag GmbH Germany, part of Springer Nature 2019

## Abstract

Acoustic streaming can be generated in microchannels by low-frequency acoustic transducer in the vicinity of sharp structures. Close to the tip, the strong curvature induces bent trajectories on the time-periodic acoustic flow, locally enhancing the streaming-generating force. In this study, we investigate the influence of the sharp structure and vibration velocity on the streaming flow. The vibration velocities are characterized by directly visualizing the displacement of tracing particles and the generated acoustic streaming is observed using particle image velocimetry, under various operating conditions. By measuring the concentration of a fluorescence dye, we evaluate the mixing performance for different values of tip angle, vibration amplitude, and flow rate through the microchannel. Our results confirm that intense streaming is generated under low-frequency (2.5 kHz) acoustic condition when the local curvature of the boundary is close to or smaller than the viscous boundary-layer thickness. It is shown that the sharpest the edge tip, the largest the vortices size and the spatial extent of the induced streaming, therefore greatly enhancing the mixing between two miscible liquids. The mixing index, linearly characterizing the mixing degree between 1 (totally separated) and 0 (perfectly mixed), jumps from 0.73 (without acoustic excitation) to 0.38 (with acoustic excitation), resulting in a highly mixed homogeneous fluid just after the sharp edge. This emphasizes the promising potential of acoustic streaming to enhance mass transfer inside microchannels which is usually limited by the laminar flow conditions.

**Keywords** Acoustic streaming · Sharp structure · Mixing performance · Fluorescence flow visualization

---

**Electronic supplementary material** The online version of this article (<https://doi.org/10.1007/s10404-019-2271-5>) contains supplementary material, which is available to authorized users.

---

✉ Xiaofeng Guo  
xiaofeng.guo@esiee.fr

✉ Philippe Brunet  
philippe.brunet@univ-paris-diderot.fr

<sup>1</sup> Univ Paris Diderot, Sorbonne Paris Cité, LIED, UMR 8236, CNRS, 75013 Paris, France

<sup>2</sup> Univ Paris Diderot, Sorbonne Paris Cité, MSC, UMR 7057, CNRS, 75013 Paris, France

<sup>3</sup> ESIEE Paris, Department SEN, Université Paris Est, 2 Boulevard Blaise Pascal, Cité Descartes, 93162 Noisy Le Grand, France

<sup>4</sup> Massachusetts Institute of Technology, 77 Massachusetts Avenue, Cambridge, MA 02139, USA

## 1 Introduction

Increasing interests in milli- or micro-fluidic devices represent both advantages and challenges. Their advantages in efficiency and compactness make them attractive for a large range of industrial (Whitesides 2006), biological, and pharmaceutical (Elvira et al. 2013) applications. However, due to geometry and pressure drop constraints, the flow regime in most micro-fluidic devices is laminar. Consequently, transport phenomena are generally considered as a challenge. Acoustic Streaming (AS) has gained interest in recent years due to its ability to generate flows even at very low Reynolds number, therefore making it advantageous in various applications (Gopinath and Mills 1994; Boluriaan and Morris 2003; Whitesides 2006; Lee and Loh 2007; Legay et al. 2012; Huang et al. 2013b, 2018b; Elvira et al. 2013).

Physically, the AS phenomenon is generated in a quiescent fluid subjected to a periodical acoustic or mechanical vibration field. A net mean flow originates from the dissipation of the vibration energy by viscosity of the fluid; the

latter can be either Newtonian or non-Newtonian. Theoretically, the phenomenon can be modeled by the time-averaged non-linear term of the Navier–Stokes (NS) equation coupled with vibration perturbation. The first AS phenomenon was observed as early as 150 years ago, but continuous research efforts have been done until today due to the diversity of mechanisms and applications (Faraday 1831; Eckart 1948; Nyborg 1953; Stuart 1966; Lighthill 1978; Boluriaan and Morris 2003).

Recently, the observation of intense flow and vortices generated by acoustic fields within sawtooth-shaped microchannels have brought a renewal of interest to boundary-driven streaming flows in micro-fluidics (Huang et al. 2013a, b, 2018a, b; Nama et al. 2014a, b; Ovchinnikov et al. 2014; Tobias et al. 2015). Huang et al. (2013a) first try to apply such type of streaming into mixing enhancement. (Ovchinnikov et al. 2014) conducted theoretical and experimental works to fundamentally investigate such a phenomenon. In their validation experiments, the sharp edge (tip of a needle) provides a 461 Hz mechanical vibration, i.e., the actuation inside the liquid. They pointed out that such streaming velocities can be of several orders of magnitude higher than Rayleigh streaming velocities under similar amplitudes of vibration. They attributed the origin of this new type of streaming to the centrifugal force around the sharp vibrating structure. For instance, in eye surgery process, the jets coming from ultrasonically vibrating needles can reach a speed of as high as 2 m/s (Zacharias and Ohl 2013). In addition to high streaming velocity, another significant characteristic of such streaming is its relatively low acoustic frequency (Huang et al. 2013a; Ovchinnikov et al. 2014) and energy input, which can be particularly adapted to transfer enhancement in micro-fluidics geometries. In the realm of acoustic excitations on microchannels, the vast majority of solutions (Bruus 2012) uses waves of a few MHz or higher frequency, so that the acoustic wavelength in water ( $\lambda_c = c/f$ , with  $c = 1430$  m/s) is of the order of the largest dimension of the channel, namely around half a millimeter or so. The most common setups use two transducers facing each other or a transducer and a reflector (Wiklund et al. 2012; Barnkob et al. 2012; Lei et al. 2013), to generate a resonance condition when the channel width is equal to the half of  $\lambda_c$ . The counterpart of this technique is the necessity to use expensive devices like high-frequency transducers or amplifiers. On the contrary, the use of sharp structures is adapted to low-frequency acoustic waves, even below the ultrasound range, typically of a few kHz, allowing the use of low-cost transducers and amplifiers. While the acoustic wavelength, of several tens of cm, is then much larger than the channel dimensions, the sharp structures induce a local intensification of the acoustic actuation to the fluid.

With the advantages of high streaming velocity and low excitation frequency, the sharp-edge acoustic streaming

could potentially efficiently improve processes such as mixing, particle selection, heat transfer, etc. Studies, especially those from Huang's group, reported the characterization of sharp-edge streaming flow and its application in mixing (Huang et al. 2013b, 2018b; Nama et al. 2014a), bio-particle and liquid-drop control (Leibacher et al. 2015; Cao and Lu 2016; Ozelik et al. 2016), as well as various on-chip devices (Huang et al. 2014, 2015a, b; Bachman et al. 2018; Zhao et al. 2019).

Although experiments and simulations on acoustic streaming in sawtooth-shaped microchannel have been done in the aforementioned studies (Huang et al. 2013b; Ovchinnikov et al. 2014), several issues remain to be investigated. In particular, the vibration conditions required to generate significant streaming need more quantitative measurements. The available literature only provides the electrical input into transducers (mainly excitation frequency and input voltage) which is not a direct physical parameter to understand the generation of streaming. Other experimental variables such as clamping, transducer type, and quality can make reproducing challenging. As a result, the physical interpretation of the fluid–wall interaction in a confined mini/micro-fluidic structure under acoustic excitation, as well as its influence on acoustic streaming generation and mass transfer performances is of both fundamental scientific interest and applicational significance.

In this study, we investigate the streaming flow properties and mixing efficiency of acoustic streaming generated in Y-shaped microchannels with sharp-edged structures. We design an experimental setup that allows to visualize streaming vortices by high-speed imaging and to investigate the key influencing parameters such as acoustic amplitudes, sharp-edge angle, as well as flow rate. A visualization based on fluorescence dye concentration tracking is used to assess the mixing performance of the Y-mixer. The paper is organized as follows: Sect. 2 summarizes the AS theory near sharp edges; Sect. 3 presents the experimental setup and the typical flow visualization; then, Sects. 4 and 5 present experimental results, respectively, on the flow properties and mixing performances, and finally, Sect. 6 concludes on the main findings as well as some perspectives.

## 2 Theoretical background

The usual framework of AS studies describes the velocity and pressure fields via a decomposition into a first-order time-periodic component and a second-order steady component, with the acoustic vibration velocity (and the subsequent induced periodic flow) being of much larger magnitude than the steady (streaming) flow response (Lighthill 1978; Rayleigh 2013).

In the time-dependent acoustic vibration field, velocity and pressure are denoted as follows:

$$\begin{aligned} V_1 &= \text{Re}(V_\omega e^{i\omega t}) \\ p_1 &= \text{Re}(p_\omega e^{i\omega t}), \end{aligned} \tag{1}$$

where  $V_\omega, p_\omega$  are the velocity and pressure variation amplitudes due to the acoustic excitation;  $V_1, p_1$  are, respectively, the first-order acoustic velocity and pressure at time  $t$ .  $Re$  means the real part of the complex terms.

The total velocity and pressure fields comprise thus two components:

$$\begin{aligned} V &= V_1 + V_0 \\ p &= p_1 + p_0, \end{aligned} \tag{2}$$

where  $V$  and  $p$  are the total velocity and pressure of fluid;  $V_0, p_0$  are the steady-flow velocity and pressure.

The sharp-edge AS in this study uses acoustic wavelength ( $\lambda_c = cf$ , in the order of  $\sim$ m) much higher than the characteristic flow dimensions (the height of the sharp edge or width of the channel,  $< 1$  mm). Both acoustic and streaming velocities are much lower than the sound speed ( $c = 1430$  m/s in water), the flow in the present study can be treated as incompressible flow. Inserting Eq. 2 into the incompressible Navier–Stokes and continuity equations leads to two relationships with time-dependent terms in Eqs. 3 and 4:

$$i\omega V_\omega = -\frac{1}{\rho} \nabla p_\omega + \nu \nabla^2 V_\omega \tag{3}$$

$$\nabla \cdot V_\omega = 0. \tag{4}$$

Averaging these two equations over a period yields to the following:

$$(V_0 \cdot \nabla) V_0 = -\frac{1}{\rho} \nabla p_0 - F_s + \nu \nabla^2 V_0 \tag{5}$$

$$\nabla \cdot V_0 = 0. \tag{6}$$

Here,  $F_s = \frac{1}{2} \text{Re}[(V_\omega \cdot \nabla) V_\omega^T]$  is the time-averaged inertia term due to the first-order acoustic field, and is treated as a steady-force term in the second-order steady equation.

Applying a spatial derivative to the first-order acoustic equations (Eqs. 3 and 4), we further reduce them to their equivalent form Eq. 7, which is the classical wave equation for the acoustic field:

$$\nabla^2 p_\omega = 0. \tag{7}$$

From the form of  $F_s$ , it is clear that a homogeneous acoustic field cannot generate any streaming flow, as the effective force would be null. However, the sharp tip structures with strong local curvature on the channel walls induce strong heterogeneity in the acoustic oscillating flow in the fluid. As sketched in Fig. 1, at a given time, the vibration of the fluid

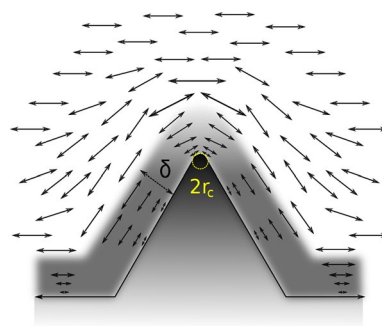


Fig. 1 Sketch of acoustic oscillating flow around a tip edge

is uniformly distributed except for the local zone around the sharp edge, the latter being the source of AS. More specifically, close to the tip, both the orientation of the acoustic field and the vibration amplitude provide favorable condition of an intense  $F_s$  very near the tip. Far from the tip, the force is null or negligible. Therefore, the non-uniformity of the acoustic field caused by the sharp structure makes acoustic streaming at relatively low frequencies (several kHz) possible. This is furtherly confirmed by our direct observation presented later in Fig. 5 as well as in the Supplementary video (Supplementary material 1).

With acoustic frequencies of the order of kHz and low-viscosity liquids like water, the dissipation length is much larger than the system size, and hence, most of the dissipation is due to the viscous friction at the solid–liquid interfaces. This friction is located in a viscous boundary layer of width  $\delta$ . (Ovchinnikov et al. 2014) point out that the streaming only appears in the situation where the radius of curvature of the walls is smaller than  $\delta$ , meaning that streaming is generated by the sharp, local gradient of velocity near the tip. Therefore, we operated with sharp tips with curvature radius of a few microns, fabricated with photolithography techniques.

As shown in Fig. 2, while no particle motion can be observed in the absence of acoustic field (Fig. 2b), a clear streaming in an extended region appears near the tip when acoustic excitation is prescribed via the transducer stuck on the glass slide (Fig. 2c). The streaming image in Fig. 2c is obtained by superposition of time sequential individual particle trajectories. Two streaming vortices are observed on both sides of the sharp edge. In the case of a round, smooth structure with big enough curvature, as shown in Fig. 2d, the acoustic streaming is not observed. While this is not strictly a parametric study on curvature diameter, the result is in accordance with Ovchinnikov et al.’s framework, demonstrating that this type of streaming should be generated with sharp structures.

Since we can briefly describe that the fluid is jetted from the tip, the resulting vortices and the strong directional

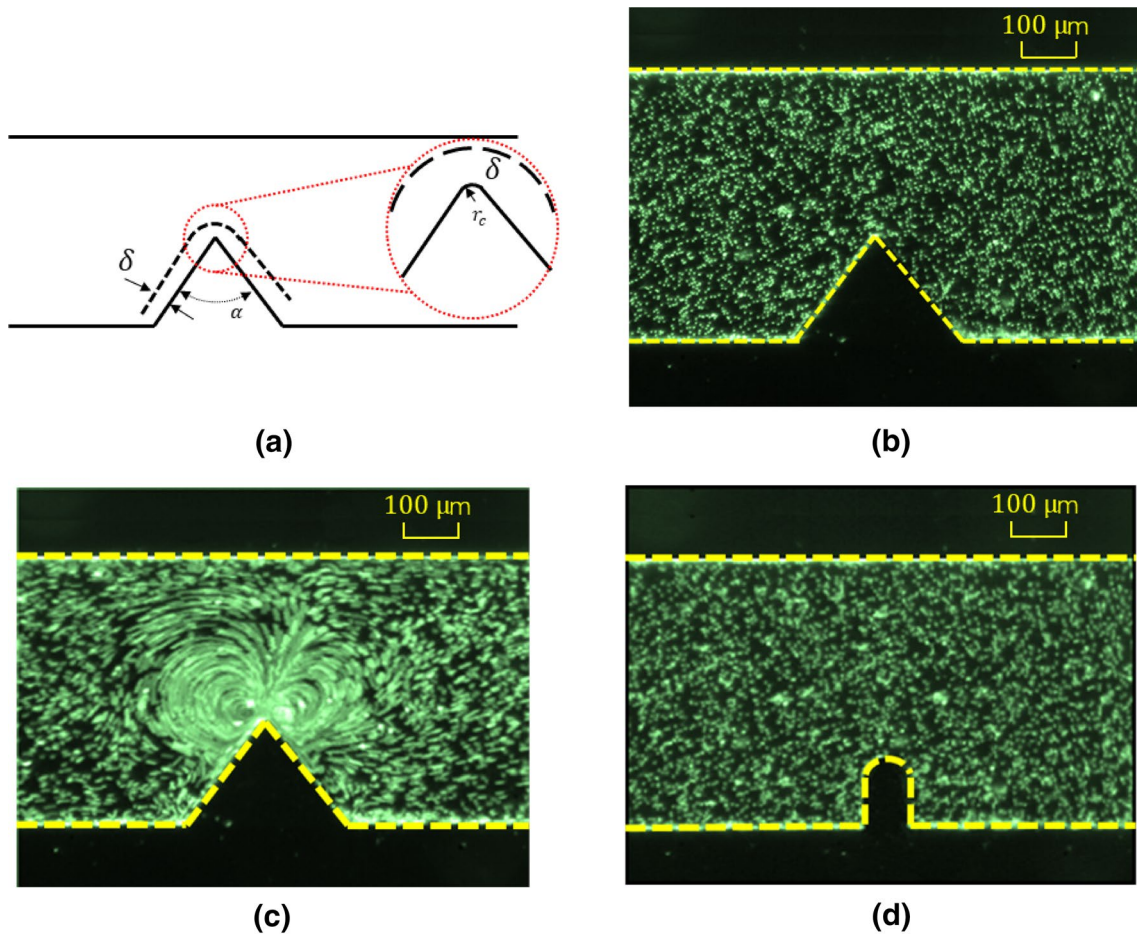


**Fig. 2** Mechanism of acoustic streaming under zero flow rate. **a** Acoustic streaming condition, sharp-edge curvature should be lower than the acoustic boundary layer  $2r_c < \delta$ ; **b** fluorescent particles distribution around a sharp-edge ( $\alpha = 60^\circ$ ) without acoustic field; **c** the streamline of the acoustic excited particles movement under a stack

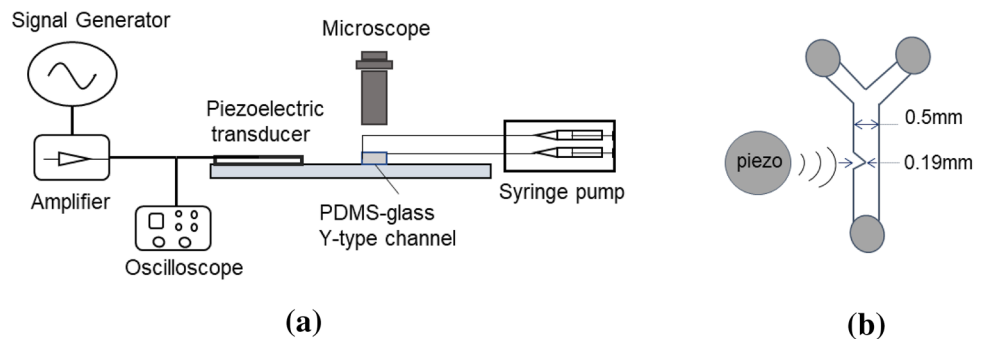
of 100 images equivalent to a duration of 100 ms,  $V_w = 37.8$  mm/s,  $f = 2.5$  kHz; **d** round edge with a curvature of  $100 \mu\text{m}$  under acoustic excitation but with no acoustic streaming,  $V_w = 37.8$  mm/s,  $f = 2.5$  kHz

flow will actively bring disturbance into the flow along the channel. The ensemble of the phenomena is potentially applicable in a large number of engineering process, such as mixing, heat transfer enhancement, etc.

### 3 Experiment and post-processing

Figure 3 shows our experimental setup as well as the micro-channel geometry. The setup around the Y-shaped micro-channel (shown in Fig. 3a) is composed of a syringe pump

**Fig. 3** Sketch of the experimental setup. **a** Fluid circulation and visualization system; **b** Y-type micro-channel with a sharp edge



(Newtown Company & Co) allowing the injection of fluid from two syringes, under well-controlled flow rate through the channel and via the two inlets. A function generator (Model 33220A Arbitrary waveform generator, Agilent) with a home-made adjustable power amplification provides input to a piezoelectric transducer (Model ABT-455-RC, RS Components). The transducer is glued on a standard glass microscope slide (width  $\times$  length  $\times$  thickness: 26 mm  $\times$  76 mm  $\times$  1 mm) through which the visualization is made using a binocular microscope together with a fast camera (MotionBLITZ Cube4, Mikrotron). The piezoelectric transducer (diameter 35 mm and thickness 0.51 mm) delivers acoustic vibrations to the glass slide and to the whole channel stuck onto it, at various resonance frequencies from about 1 kHz up to 40 kHz. We chose to operate at one of these resonance peaks  $f$ , namely that at  $f = 2.5$  kHz. It turns out that the best operating conditions in terms of streaming flow were obtained at this frequency.

The Y-shaped Polydimethylsiloxane (PDMS) channel is designed by 2D photolithography. First, a mold made of SU8 negative photoresist was fabricated: a 50  $\mu\text{m}$ -thick SU8 liquid layer was spin-coated on a silicon wafer. After a soft baking at 65  $^\circ\text{C}$ , the resist was exposed to UV through a photomask. The resist was then immersed in a developer bath and then hard-baked at 95  $^\circ\text{C}$ . Then, PDMS (Sylgard 184) was thoroughly mixed with 10% in mass of curing agent, degassed in a vacuum chamber, and poured on the SU8 mold to constitute a 2.5-mm-thick layer of PDMS mixture on top of the wafer. The whole is put in a stove at 65  $^\circ\text{C}$  during 4 h.

The PDMS is then sealed and stuck on a glass microscope slide after a 1-min oxygen plasma treatment of both sides. The microchannel of a height of 50  $\mu\text{m}$  is then formed between the PDMS and the glass slide. The plasma treatment enables the microchannel to withstand the pressure from inlets without leakage. Key geometrical dimensions of the Y-mixer are detailed in Fig. 3b. Sharp edges with different angles  $\alpha$  (30 $^\circ$ , 60 $^\circ$ , 80 $^\circ$ , and 90 $^\circ$ ) were fabricated from various molds. Hence, all channels were sealed on a similar glass slide, and rapid cure epoxy resist was used to permanently glue the transducers on each glass slide. It turns out that the best acoustic coupling was obtained this way. The radius of curvature of the different tips was measured with a 120X microscope with five repetition measurements of each angle. According to our measurement of the curvature diameter  $2r_c$  of the sharp edge, its value ranges from 2.8 to 10.3  $\mu\text{m}$ , which are shown in Fig. 4 and Table 1. These values are all smaller than the viscous boundary layer thickness 11.5  $\mu\text{m}$ , determined by  $\delta = \sqrt{2\nu/\omega}$  (Boluriaan and Morris 2003), with  $\nu$  the kinematic viscosity of the fluid, and  $\omega$  the angular frequency.

Two syringe pumps provide equal flow rate  $Q_s$  through the two PDMS microchannel inlets. It should be noted that hereafter the channel throughput  $Q_c$  is defined as the flow

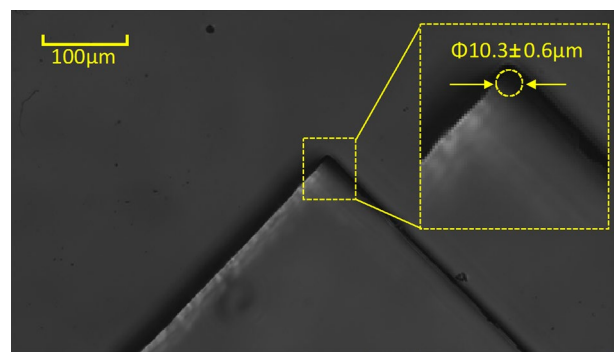


**Fig. 4** Measurement of the curvature diameter under a  $\times 120$  microscope, here  $\alpha = 90^\circ$

**Table 1** Curvature diameter corresponding to different tip angles of the sharp edges

Sharp edge angle $\alpha$ ( $^\circ$ )	30	60	80	90
Curvature diameter $2r_c$ , ( $\mu\text{m}$ )	$2.8 \pm 0.3$	$5.8 \pm 0.4$	$7.1 \pm 0.4$	$10.3 \pm 0.6$

rate in the main channel. It is the sum of the two single inlet flow rates provided by each syringe ( $Q_s$ ).

The transducers are excited with periodic sinusoidal signal. The available range of peak-to-peak voltage is between 0 and 30 V (up to  $\pm 15$  V). It is important to notice that the speed of sound ( $c$ ) in water is 1430 m/s and that in glass is 4540 m/s, so the wavelengths of vibration ( $\lambda = c/f$ ) at 2.5 kHz are, respectively, 0.57 m and 1.82 m. These values are far greater than the scales of the channel, whose width is 0.5 mm and length is 25 mm. The amplitude of the acoustic wave is, therefore, expected to be uniform in the whole channel.

To visualize the flow, the fluid is seeded with fluorescent particles (green polystyrene microspheres, diameter 4.9  $\mu\text{m}$ , Thermo Scientific). However, due to the limited sensitivity of the high-speed camera, the best contrast and image quality is obtained by direct lighting with white light, hence with the diffused light instead of the fluorescence-emitted light. To enhance the contrast, a cold-light beam shines from the bottom of the glass slide. The depth of field of the microscope lens is about 10  $\mu\text{m}$ , five times smaller than the channel depth (50  $\mu\text{m}$ ). Hence, after careful focal adjustments (based on finding the position that shows the maximal transverse velocity for a given flow rate), we obtain high fidelity pictures with clear focus, as shown in Fig. 2b–d.

Since the streaming velocity near the tip can be of comparable magnitude to the vibration velocity, which is different from most previous studies (Squires and Quake 2005) and will be discussed later (Sect. 4.3.2), another challenge is to observe and measure these two velocities separately. The

following methods are used: first, to detect the motion of the particles during one vibration period and compute the streaming velocity, the frame rate of the camera is set to as high as 25 kHz and the exposure time as short as 25  $\mu\text{s}$ . Under this condition, any individual particle appears as a small sphere of a few pixels, because the exposure time is much smaller than the vibration period ( $1/f = 400 \mu\text{s}$ ). A total of ten pictures are captured for every vibrating cycle, making the visualization of the acoustic vibration possible. To obtain the streaming velocity, we choose sequential images with a time interval of one acoustic period to “hide” the vibrational velocity. Then, to measure the acoustic vibration velocity  $V_\omega$ , the frame rate of the camera is reduced to 2.5 kHz with an exposure time extended to 400  $\mu\text{s}$ . Under this condition, particles in these pictures appear as threads of fixed length that corresponds to the amplitude of its acoustic-driven motion (Fig. 5). Results are shown in supplementary video. During the experiment, the pictures are continuously synchronized with the camera to the computer.

The obtained images are then treated with open-source software ImageJ (Schneider et al. 2012). For vibration velocity, the particles’ displacements are directly measured from the captured images, and the results as well as the uncertainties are discussed in detail in Sect. 4.2. For the streaming field, the relative displacement of particles at a given phase of the vibration period and at given locations allows the determination of the velocity field. Successive frames are converted into an array of displacement vectors for each particle by the software PIVlab (Thielicke and Stamhuis 2014). Second, summing the intensity of the images of a number of frames allows clear visualization of trajectories and then the location, form, and sizes of vortices.

Besides, COMSOL Multiphysics © simulation is used as a control study to verify the reliability of the PIV result in terms of velocity characterization. The control study is done without acoustic excitation using a standard laminar flow model. The results are shown to be highly close (See Supplementary material 2).

## 4 Results and discussion

### 4.1 From acoustic vibration to AS

The direct visualization of fluid motion responding to the acoustic forcing is shown in Fig. 5a and the supplementary video. The main image Fig. 5 is obtained from acquisitions with high-speed imaging (1.25 kfps) of particle trajectories over a few vibration periods. No apparent motion of the microchannel walls could be evidenced from these visualizations. Hence, the analysis of individual traces left by particles gives both the amplitude of the acoustic wave in the fluid and the orientation of this field  $V_\omega$ . Besides the

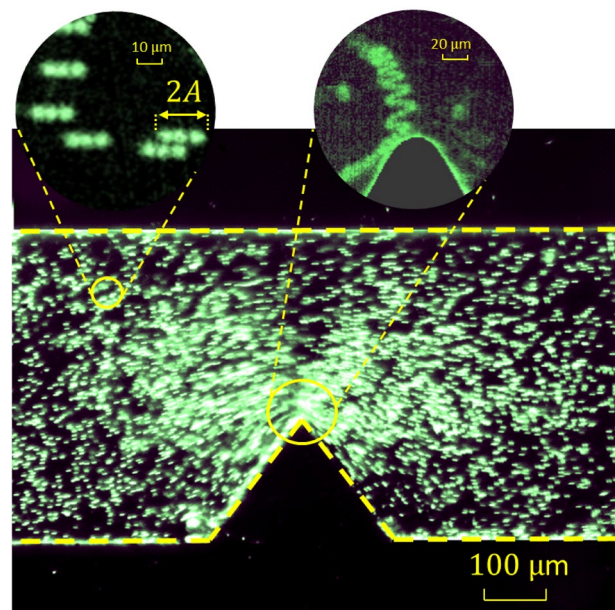


**Fig. 5** The mechanism of acoustic streaming explained by high-speed visualization of acoustic vibrations within the fluid, from particle trajectories over a few periods; the velocity measured is 101.7 mm/s (see Supplementary video for dynamic visualization effect)

main image, two magnified details are shown on top of it. On the left of Fig. 5, we show the particle vibration by taking six images within one vibration period. This allows the quantification of the acoustic vibration amplitude  $2A$ . On its right, the trajectory of one particle during ten periods is followed. This picture shows that near the tip, the streaming velocity  $V_0$  (in the direction of the sharp tip, shown as vertical) has a magnitude comparable to the vibration velocity  $V_\omega$  (in the direction of the fluid channel, shown as horizontal). Similar to the idealized sketch of the amplitude and direction of this first-order flow in Fig. 1, far enough from the viscous boundary layer, the amplitude is found constant and the fluid displacement is parallel to the channel walls where the oscillating fluid movement is possible. However, due to the no-slip boundary condition along the wall, the viscous shear develops within the layer of thickness  $\delta$  along the walls and this amplitude vanishes within this boundary layer. Furthermore, the orientation of the acoustic fluid motion has to locally match that of the walls. Consequently, the acoustic velocity field  $V_\omega$  is subjected to sharp variation of orientation around the tip. Furthermore, the acoustic amplitude is higher near the tip than elsewhere in the channel, as shown in Fig. 5. As emphasized in (Ovchinnikov et al. 2014), this leads to an intense streaming force  $F_s$  very near the tip, while this force is null or negligible far from the tip. Therefore, the non-uniformity of the acoustic field caused by the sharp structure makes acoustic streaming at relatively low frequencies (several kHz) possible.

### 4.2 Acoustic vibration speed

As the transmission from electrical transducer power to the solid glass then to the fluid is rather complex (Uchida et al. 1995), we here only experimentally characterize the resulted vibration. Therefore, the vibration amplitude and velocity induced by the transducer are measured directly on the glass slide and indirectly in the fluid, the former by a laser vibrometer, and the second by particle visualization. Their comparison allows us to identify the relative oscillation velocity on the fluid–solid interface, where the acoustic streaming develops.

On one hand, a laser vibrometer (OFV-505 model, Polytec) is used to directly measure the vibration on the glass slide—near the location of the channels and after the PDMS bonding. Within the uncertainties of measurements, the relationship between the prescribed voltage and the local vibration velocity  $V_{\omega, \text{glass}}$  is found to be linear. We measured for instance  $V_{\omega, \text{glass}} = 2.2 \text{ mm/s}$ ,  $4.4 \text{ mm/s}$ , and  $6.9 \text{ mm/s}$  corresponding, respectively, to input peak-to-peak voltages  $U_{\text{pp}}$  of 10, 20, and 30 V, at 2.5 kHz. In terms of acoustic amplitude  $A_{\text{glass}}$ , such that  $V_{\omega, \text{glass}} = A_{\text{glass}}\omega$ , and as  $f = 2.5 \text{ kHz}$ , it corresponds to displacement of the order of 1 micron or smaller on the glass.

On the other hand, acoustic fluid displacement  $2A$  is extracted from high-speed imaging, as already shown in Fig. 5. Figure 6 shows the linear relation between induced vibration velocity of the particles inside the liquid and the peak-to-peak voltage of the piezo-transducer, which is consistent with (Franke et al. 2003). The error of measuring the vibration velocity mainly comes from the pixel resolution and uncertainties of  $2A$  are within 1 pixel (representing  $0.75 \mu\text{m}$ ) which corresponds to  $\pm 6.1 \text{ mm/s}$ . For instance,

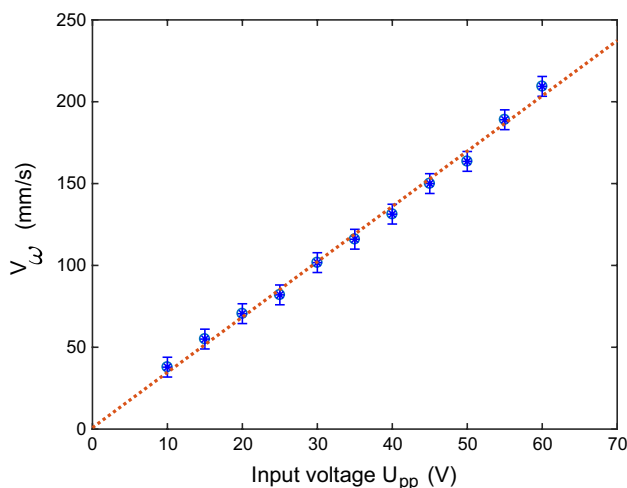


**Fig. 6** Acoustic vibration velocity measured by particle visualization at different input peak-to-peak voltage of the piezo-transducer. The calibration is given by the linear fit  $V_{\omega} = aU_{\text{pp}}$ ,  $a = 3.38 \text{ mm}/(\text{s} \cdot \text{V})$

our results show values of the particles acoustic vibration velocity  $V_{\omega} = 37.8 \text{ mm/s}$ ,  $50.5 \text{ mm/s}$ ,  $70.5 \text{ mm/s}$ ,  $85 \text{ mm/s}$ , and  $101.7 \text{ mm/s}$  at 2.5 kHz and corresponding to a peak-to-peak voltage  $U_{\text{pp}}$  of 10 V, 15 V, 20 V, 25 V, and 30 V, which will be the main experimental conditions of the present study. For higher vibration amplitudes with transducer inputs between 30 and 60 V, the vibration velocities are also shown in Fig. 6. However, due to experimental limitations (mainly exposure time of the fast camera in case of very high streaming velocity), our experimental conditions are only limited to under 30 V.

Since only the relative fluid–wall vibration accounts for the acoustic streaming phenomenon, and considering the measured solid vibration is lower than the tenth of the liquid vibration, hereafter, we use the particles visualization-based vibration speed as the reference, i.e.,  $V_{\omega}$ . The following discussions are all based on this reference (Fig. 6).

### 4.3 Flow visualization

In this section, we keep the piezoelectric transducer input to 2.5 kHz and use three different vibration velocities:  $V_{\omega} = 37.8 \text{ mm/s}$ ,  $70.5 \text{ mm/s}$ , and  $101.7 \text{ mm/s}$ . Different tip angles  $\alpha$  are used:  $30^\circ$ ,  $60^\circ$ ,  $80^\circ$ , and  $90^\circ$ , so as to different channel flow rates  $Q_c = 0, 1, 4, 8, 12, 16 \mu\text{L}/\text{min}$ . We focus our following discussions on how the acoustic streaming disturbs the main flow.

#### 4.3.1 General characteristic of the flow

Acoustic perturbation to the fluid can be clearly observed from the velocity field given by the PIV. As shown in Fig. 7a, under an acoustic vibration of  $V_{\omega} = 37.8 \text{ mm/s}$  at 2.5 kHz, the fluid around the sharp edge is jetted from the tip through the transverse direction of the microchannel. Since no throughput is imposed in that case, two symmetrical vortices appear besides the sharp edge. Outside of the region near the sharp edge (shown in the red square in the upper right corner of Fig. 5a), however, no fluid disturbance is observed, confirming that AS originates from the geometrical singularity of the tip. As already discussed in Fig. 2d, for the “round” structure with  $2r_c = 100 \mu\text{m} \gg \delta$ , there is no evident streaming appearing around the structure. This confirms the hypothesis given by the perturbation theory (Ovchinnikov et al. 2014), that only when the tip curvature is narrower than the acoustic boundary layer, that the acoustic streaming could appear.

Indeed, considering  $F_s = \frac{1}{2} \text{Re}[(V_{\omega} \cdot \nabla) V_{\omega}^T]$ , it is clear that the stress is stronger in areas where the spatial variations of  $V_{\omega}$  are sharper. Hence, the streaming vortices around the sharp structure can be attributed to the periodical curved motion of the fluid around the tip. The streaming force  $F_s$  generates a jet from the tip, perpendicular to the channel

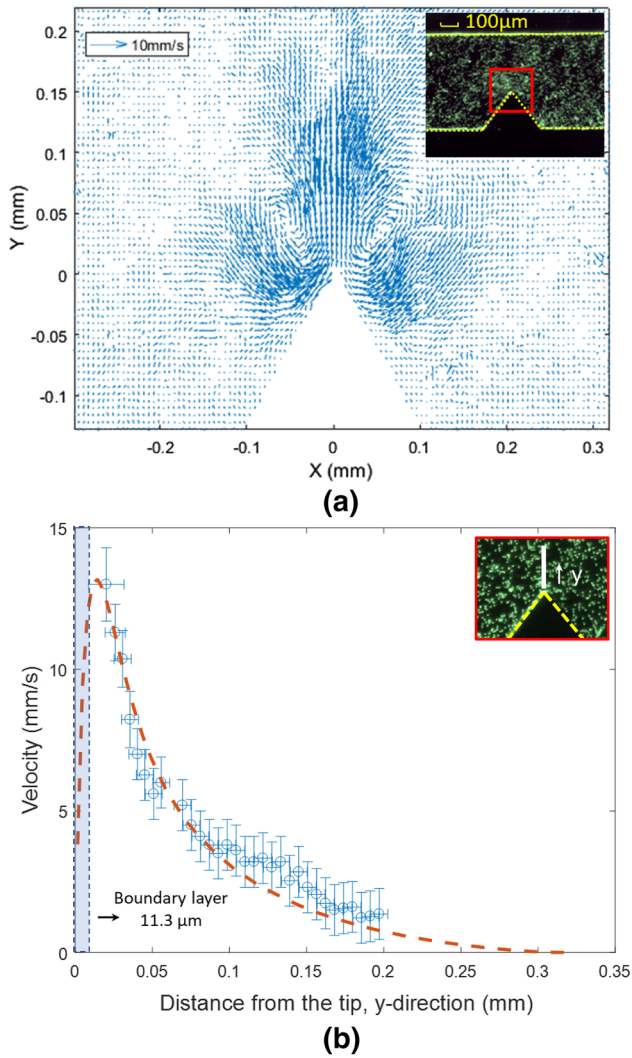


**Fig. 7** Acoustic streaming velocity field, at  $V_\omega = 37.8$  mm/s and  $f = 2.5$  kHz. **a** Velocity field obtained from PIV and **b** velocity distribution along the transverse direction from the tip. The acoustic streaming is obtained from a tip with  $\alpha = 60^\circ$ ,  $Q_c = 0$ . The red line shows qualitatively the velocity evolution profile which is in accordance with the simulation results by (Ovchinnikov et al. 2014)

longitudinal direction, which in turn induces the aforementioned vortices' pair.

In Fig. 5b, we trace the velocity distribution along the y-direction (following the thick white line shown in the upper right corner,  $y=0$  is taken at the tip) based on the PIV results. It clearly shows a rapid increase of the AS velocity from zero to a maximum value in a distance as short as 0.025 mm. After the peak, the AS velocity reduces gradually as its momentum transfer to the main fluid in the channel. The sharp decrease of the streaming velocity is consistent with Ovchinnikov's estimation (Ovchinnikov et al. 2014), the force is localized within a distance of less than  $\delta$  from the tip; therefore the velocity along y-direction decreases

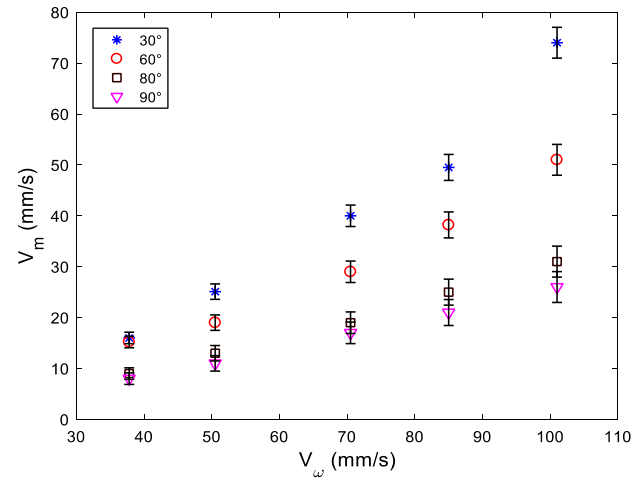


**Fig. 8** Maximum streaming velocity versus acoustic velocity, generated near sharp tips of different angles, under no-flow condition ( $Q_c = 0$ )

locally and rapidly after reaching the maximum value. Under the above condition, the peak value (maximum AS velocity) is  $V_m = 15.4$  mm/s and it depends significantly on the excitation amplitude, sharp-edge angle, etc. It should be noted that uncertainties of streaming velocity mainly come from two aspects: the first is the coupling of the acoustic vibration with the streaming, which primarily concerns the maximal velocity value  $V_m$ , and the second lies in the pixel resolution. For the first, the error of  $V_m$  is proportional to the streaming velocity and is estimated to be  $\pm 3\%$  of  $V_\omega$ . For the second, the pixel resolution (1 pixel =  $0.75 \mu\text{m}$ ) during two sequential images of a time slaps of  $400 \mu\text{s}$  results in an error of  $\pm 0.9$  mm/s.

#### 4.3.2 Maximum acoustic-induced streaming velocity

As a signature of the acoustic streaming intensity, we extract from each velocity field the transverse component  $V_m$  of the maximum velocity along the tip axis, as shown in Fig. 5b.

Figure 8 illustrates the influence of acoustic velocity  $V_\omega$  and tip angles  $\alpha$  of the sharp edge on the maximum AS velocity  $V_m$ . Sharper edges and stronger acoustic excitation lead to higher maximal velocity. Under our test conditions, the highest maximum AS velocity is 73 mm/s and it appears at  $V_\omega = 101.7$  mm/s (peak-to-peak voltage of 30 V) with the sharpest edge angle  $30^\circ$  (with  $2r_c = 2.8$  microns). This confirms that the two velocities are in the same order of magnitude, with a ratio of  $V_\omega/V_m = 1.2$ . Under lower acoustic excitation, the AS effect is lower and the ratio becomes  $V_\omega/V_m = 1.7$  ( $V_\omega = 37.8$  mm/s,  $V_m = 20$  mm/s, for the  $30^\circ$  sharp edge). The fact that  $V_\omega$  and  $V_m$  are not linearly related is consistent with Ovchinnikov et al.'s theory (Ovchinnikov et al. 2014). However, the framework of their work



is  $V_\omega \gg V_m$ , and hence, a quantitative agreement with our results should not be expected. Furthermore, higher streaming velocities are found for structures with sharper tip and smaller angle. This is consistent with that sharper tips lead to stronger Rayleigh stress near the tip, for the same vibration velocity and confirms previously observed trends (Nama et al. 2014b).

Let us note that the above conclusion is based on results  $Q_c = 0$ . When  $Q_c > 0$ , the streaming vortex is strongly influenced and a detailed visualization on the vortex shapes is necessary.

#### 4.4 Vortex shape, size, and flow disturbance

From Fig. 9a, which illustrates the particle trajectories at  $Q_c = 0$ , it is clear that the acoustic streaming originates from the sharp edge and induces two counter-rotating symmetrical vortices. These vortices have significant spatial extension: the disturbance can extend even to the other side of the channel, where streams initially flowing in the centerline

are dragged to the side of the sharp edge. Furthermore, when  $Q_c > 0$ , the symmetry of the two vortices is broken (Fig. 9b–d). Due to longitudinal convection of momentum, both vortices on the upstream and downstream side shrink at moderate-flow rate, generally not in a perfectly symmetric way. With the presence of unidirectional main stream, the vortices on the downstream are less impacted than the upstream ones (Fig. 9c, d). For instance, at a flow rate of 12  $\mu\text{L}/\text{min}$ , the vortex downstream can still exist, while the upstream one completely disappeared. Therefore, the influence of acoustic vibration on the flow, and in particular the relative importance of the traverse streaming velocity component, vanishes at very high flow rates. Let us underline that the maximal throughput flow rate (12  $\mu\text{L}/\text{min}$ ) corresponds to an averaged longitudinal velocity of about 1 cm/s which, except very near the tip, is generally much larger than the transverse component of the streaming velocity.

To quantify the disturbance of the streaming flow to the main flow  $Q_c$ , vortex size and disturbance distance are measured. For each experimental condition, five repeated

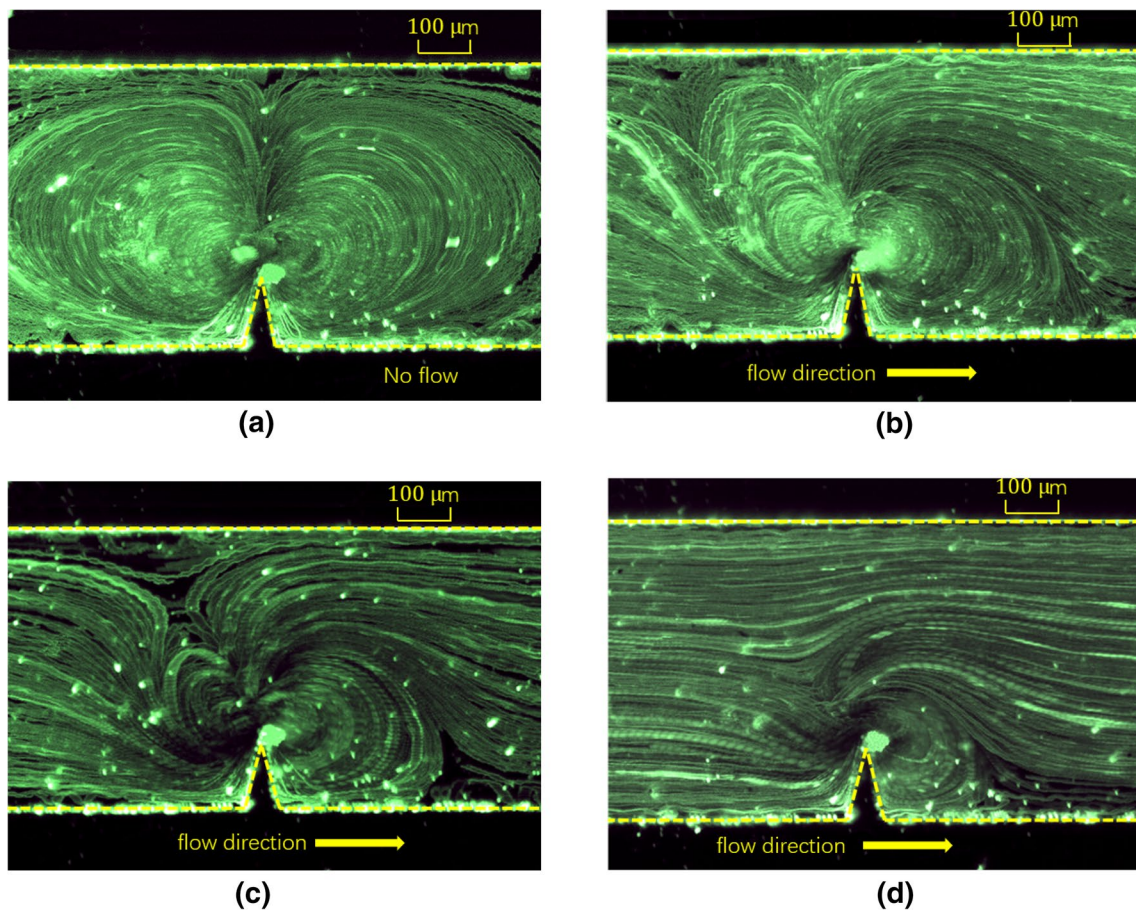


**Fig. 9** Flow visualization near the sharp tip, using particle trajectories at different channel throughputs, experimental conditions:  $\alpha = 30^\circ$ ,  $V_a = 101.7 \text{ mm/s}$  and  $f = 2.5 \text{ kHz}$ . The flow direction is from left

to right. Flowrate: **a**  $Q_c = 0$ , **b**  $Q_c = 4 \text{ L/min}$ , **c**  $Q_c = 8 \text{ L/min}$ , and **d**  $Q_c = 12 \text{ L/min}$

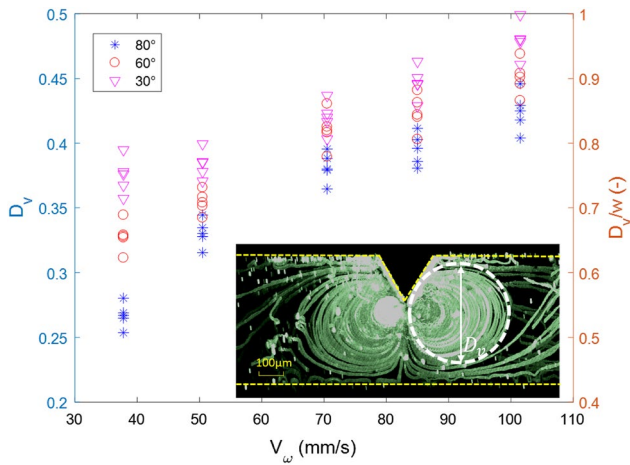


**Fig. 10** Vortex size  $D_v$  and its relative value to the channel width  $D_v/w$ , versus acoustic vibration velocity, at zero flowrate around different sharp edge angles and acoustic stimulations. Condition: with  $\alpha = 30^\circ, 60^\circ, 80^\circ$   $Q_c = 0$ ,  $V_\omega = 37.8, 70.5$  and  $101.7$  mm/s, and  $f = 2.5$  kHz;  $w = 0.5$  mm means the total width of the channel

measurements are conducted with the acoustic excitation. In addition, for each measurement, 1000 images (5 s) are stacked to assure that the vortex reaches a steady size and uncertainties mainly come from the pixel resolution and particle density near the interface area.

Figure 10 shows, for the case  $Q_c = 0$ , how the vortex size varies with different acoustic velocity  $V_\omega$  and tip angle  $\alpha$ . The vortex size,  $D_v$ , is defined as the diameter of vortices appearing, respectively, at the upstream and downstream side of the sharp edge. For the particles outside the circle, their motions are only driven by inertia force of the main flow instead of the acoustic streaming. Hence,  $D_v$  characterizes the maximum area influenced by the streaming. As the two vortices are symmetrical, we do not distinguish the upstream and the downstream vortex size.

The vortex size takes larger values for stronger vibration velocities, and for a sharper tip angle (smaller diameter than curvature): this is consistent with the similar trends observed for the maximal streaming velocity. At  $V_\omega = 101.7$  mm/s and  $\alpha = 30^\circ$ , the vortex size can reach 0.48 mm. As  $V_\omega$  increases, the acoustic streaming spreads over the whole channel width ( $D_v/w$  approaches 1) for almost all tip angles tested. In such a situation, the vortex size is limited by the microchannel width. On the other hand, with low acoustic excitation, only sharp edge with smaller angle can help to achieve big vortices: at  $V_\omega = 37.8$  mm/s, the value of  $D_v/w$  can reach 0.76 for the  $30^\circ$  tip but only 0.27 for the  $80^\circ$  one.

Figure 11 shows the variation of vortex size at both downstream and upstream of a  $30^\circ$  tip, under different flow rates. As the flow rate increases from null to  $1 \mu\text{L}/\text{min}$ , the vortices size reduces drastically from 0.42 to 0.29 (upstream) and 0.26 (downstream). The vortices continue

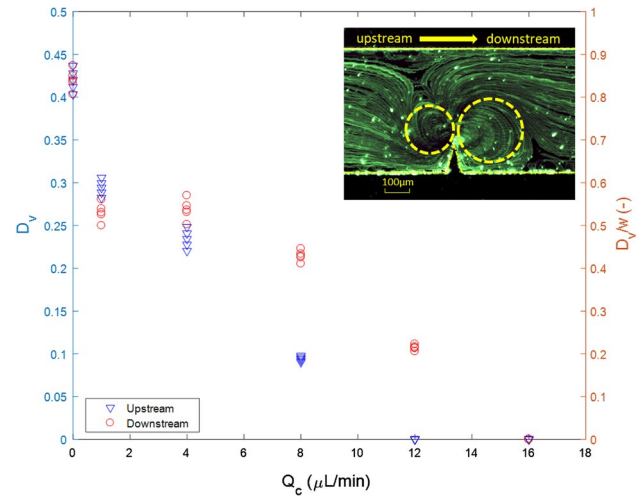


**Fig. 11** Upstream and downstream vortex size ( $D_v$  and  $D_v/w$ ) at different flow rates. Condition:  $\alpha = 30^\circ$ ,  $V_\omega = 70.5$  mm/s, and  $f = 2.5$  kHz

to shrink after  $4 \mu\text{L}/\text{min}$  and they totally disappear when the flow rate is higher than  $16 \mu\text{L}/\text{min}$ . In most cases, the upstream vortex is smaller than the downstream one, i.e., between 4 and  $16 \mu\text{L}/\text{min}$ . However, results suggest that there is a threshold of flow rate around  $2 \mu\text{L}/\text{min}$  under which the upstream vortex is even larger than the downstream one. A possible underlying reason is that the main stream velocity is lower than the upstream longitudinal AS velocity coming from the counter-flow direction. In such a situation, part of the fluid of the upstream vortex still flows back to the sharp edge, enhancing the vortex development. Otherwise, the fluid goes away with the main flow, thus reducing the vortices size. At higher throughput, comparatively, the downstream vortex varies relatively more slowly with flow rate and is subjected to less influence from main flow, presumably because the vortex is squeezed into the low-pressure area formed by the sharp structure. Although there still exists the upstream vortex at large throughput, it plays little role on the main flow.

From the point of view of transverse mass transfer in the channel, we introduce the disturbance extension  $D_{\text{dis}}$  to quantify the perturbation of the streaming on the main flow. The identification of  $D_{\text{dis}}$  requires the definition of a critical streamline, as shown in the sub-Fig. 12. The critical streamline (Wang et al. 2012) separates an active perturbation zone (between the tip and the critical line, most of the fluid pass by the tip and then jetted out) and a passive zone (out of the critical line, only a distortion of the main flow is witnessed). As illustrated in Fig. 12, the flow remains laminar in the passive zone while highly perturbed in the active one. The  $D_{\text{dis}}$  is defined as the distance from the tip to the tangential limit of the critical streamline.

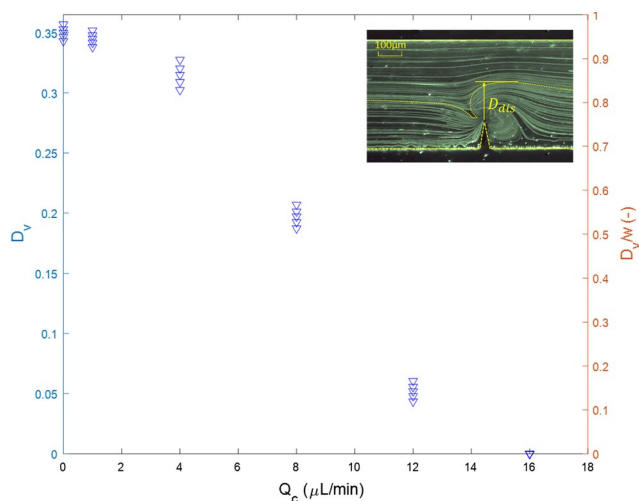


**Fig. 12** Disturbance extension  $D_{dis}$  as a function of channel throughput. Conditions:  $\alpha = 30^\circ$ ,  $V_\omega = 70.5$  mm/s, and  $f = 2.5$  kHz

Relative value is also defined for the disturbance extension with respect to the transverse distance from the tip, noted as  $RD_{dis}$ :

$$RD_{dis} = \frac{D_{dis}}{w - h_v}, \tag{8}$$

where  $w = 0.5$  mm is the channel width, and  $h_v = 0.18$  mm represents the tip height.

As shown in Fig. 12, despite that the upstream vortex may disappear, the disturbance extension might not be zero. At high flow rates like 12  $\mu\text{L}/\text{min}$ , the perturbation could reach 14% of the channel ( $RD_{dis} = 0.14$ ). To sum up, the flow perturbation is closely coupled with the flow rate and the disappearance of vortices does not mean no acoustic streaming occurs. Channel throughput should be considered as a critical parameter that is coupled with acoustic streaming. Particularly, at high flowrate, vortices are either easily flushed or are fully shadowed in the main stream.

### 5 Mixing performance

From the above analyses, we expect that the acoustic streaming brings active disturbance into the channel flow, especially at low flow rate and high vibration velocity. To confirm this, we performed mixing experiments using two miscible fluids. One is deionized water and the other is deionized water filled with fluorescent blue dye (Methylene Blue, Fisher Scientific S.A.S.). By observing the variations of the concentration of the blue dye across the channel width and measuring the mixing extent along flow direction, we assess the effect of acoustic excitation on the mixing process.

As a reference, the same flow condition but without acoustic excitation is used for comparison. Besides, several flow rate scenarios are tested based on identical single inlet flow rates  $Q_s$ , which equals  $\frac{1}{2}Q_c$ . The following discussions are based on  $Q_s$ .

Figure 13 shows how the normalized concentration (in Eq. 9, based on Beer–Lambert law) across the transverse direction of the channel evolves at different locations. One location A1 before and two locations A2–A3 after the sharp edge are sampled. We observe that at A1 ahead of the sharp edge, the two fluids begin to mix with each other driven by the upstream vortex. At the sharp edge position, the mixing process is furtherly improved by the intense jet. After the sharp edge, the mixing process is no longer influenced by the acoustic streaming and, therefore, only mass diffusion contributes to mixing, as shown between A2 and A3 in Fig. 13.

The enhancement of the mixing process around the sharp edge can be divided into two steps: (i) the upstream vortex pushes some (high-concentration) fluid against the main flow, directly making it into contact with the other stream; (ii) the fluid jetted by the sharp structure as well as the downstream vortex furtherly disrupt the mixing interfaces. To quantify the mixing, we introduce the mixing index  $M$  along the flow direction (Eqs. 9 and 10):

$$C_n = \ln \frac{I_0}{I} \bigg/ \frac{I_0}{I_b}; \quad C_n \in [0, 1] \tag{9}$$

$$M = \sqrt{\frac{\frac{1}{N} \sum_{i=1}^N (I_i - I_m)^2}{I_m^2}}, \quad M \in [0, 1], \tag{10}$$

where  $C_n$  stands for the normalized concentration;  $I_0$  is the gray value of pure water;  $I_b$  is the gray value of the unmixed blue dye liquid;  $I$  is the gray value of pixels. In Eq. 10,  $I_i$  is the gray value of  $i_{th}$  pixel;  $I_m$  is the average gray value of  $N$  pixels. In this study,  $I_m$  is the average gray value of pixels across the width of the channel at certain pixel position along flow direction.

Errors of the Mixing Index in this study are mainly caused by dye deposition near the channel border both on the glass slide and on the PDMS. For every experimental condition, five repeated measures under the same experiment setup are conducted and the maximum error for Mixing Index is 0.02.

As shown in Fig. 14, without acoustic excitation and as a result of the sole diffusion, the mixing index slowly decreases. At  $V_\omega = 70.5$  mm/s, the mixing index decreases from 0.8 to 0.6 while crossing the sharp structure and at  $V_\omega = 101.7$  mm/s, it furtherly decreases from 0.78 to 0.4. Therefore, the stronger the acoustic excitation, the higher the mixing index obtained. It is obvious that the mixing process within the vicinity regions ahead and after the sharp structure is accelerated by the upstream and downstream vortices

**Fig. 13** Concentration field across the microchannel section in the nearby area before and after the sharp edge. X-axis is the normalized concentration  $C_n$  (values 0 and 1 represent two different fluids, 0.5 means complete mixing); Y-axis is channel width. Conditions:  $\alpha = 30^\circ$ ,  $V_\omega = 70.5 \text{ mm/s}$ ,  $f = 2.5 \text{ kHz}$  and  $Q_s = 0.5 \text{ }\mu\text{L/min}$

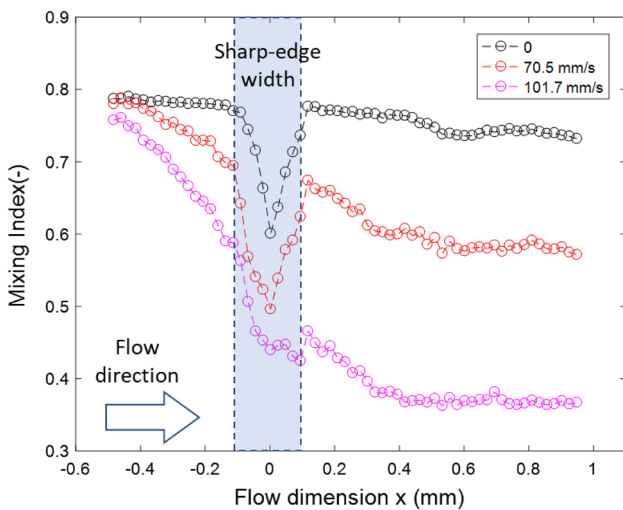
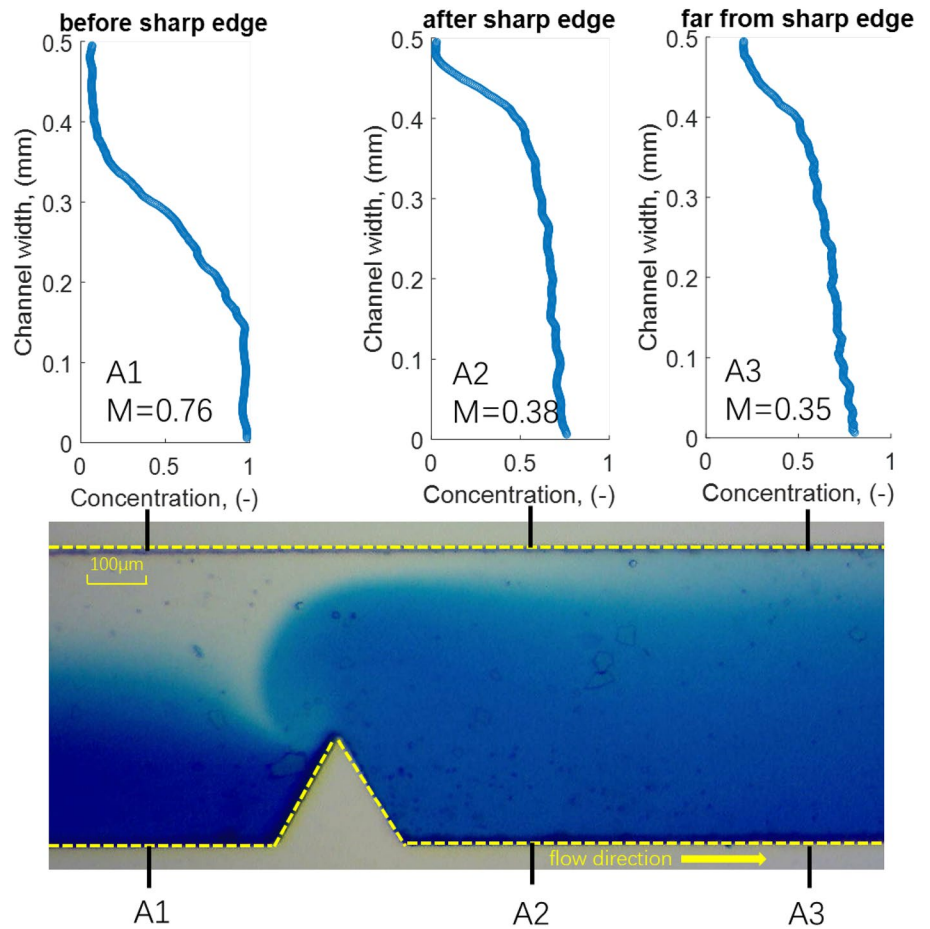


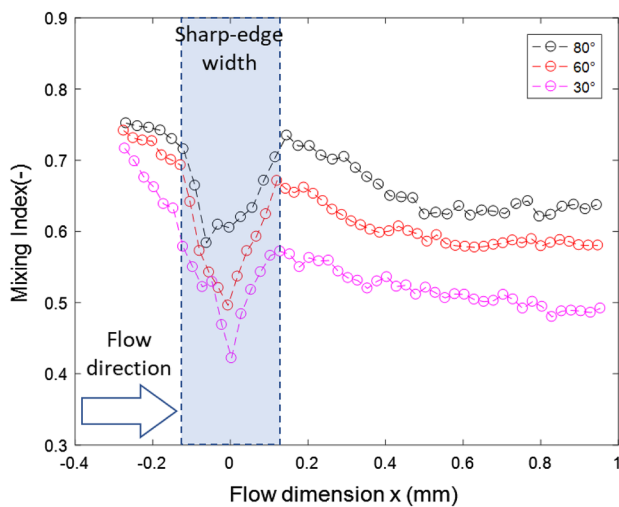
**Fig. 14** Mixing index at different acoustic excitation amplitudes. Conditions:  $\alpha = 30^\circ$ ,  $Q_s = 2 \text{ }\mu\text{L/min}$ , and  $f = 2.5 \text{ kHz}$

discussed above. Actually, diffusive mixing happens before the sharp edge, so the mixing index does not start from 1 in the figures.

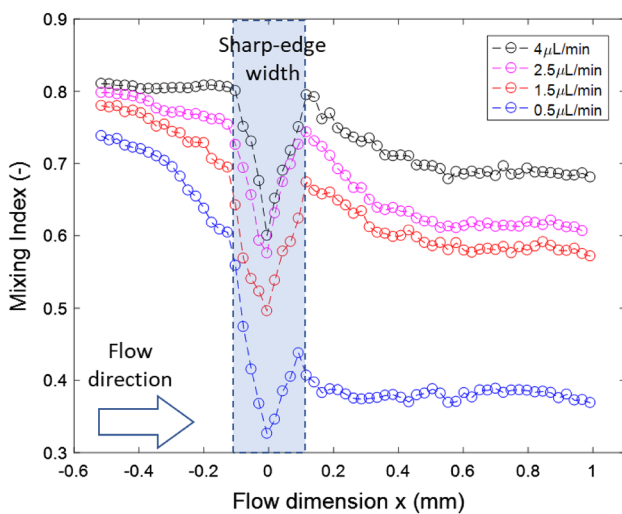
It should be noted that the width of the channel can influence the calculation of the Mixing Index, so the values within the shadow (beside the sharp edge) in Fig. 14 cannot be reliable criteria of the mixing. Only values before and after sharp edge are directly comparable.

Figure 15 shows the mixing index as a function of different tip angles. Sharper angles clearly allow better mixing degree at the outlet, since the mixing index drops from 0.7 to 0.52 for the  $30^\circ$  tip but only to 0.65 for the  $80^\circ$  one. This is consistent with the stronger streaming effect, in terms of vortex diameter and disturbance extent, with sharper tips.

The influence of the flow rate  $Q_s$  on the mixing performance is shown in Fig. 16. When the inlet flow rate increases from 0.5 to 1.5  $\mu\text{L/min}$ , the mixing index at the outlet turns from 0.38 to 0.6, thus reducing the mixing degree. In case of even higher flow rate at the same acoustic condition, the mixing continues to degrade. For example, with a flow rate of  $Q_s = 4 \text{ }\mu\text{L/min}$ , the mixing index is only achieved to 0.68. Above 1.5  $\mu\text{L/min}$ , the effect of acoustic streaming on the mixing performance can be considered negligible. The short fluid residence time in the channel (Guo et al. 2018) in cases of high flow rate seriously weakens the mixing efficiency at the outlet. To sum up, with low flow rate, one single acoustically excited sharp edge can



**Fig. 15** Mixing index at different tip angles of the sharp edges. Conditions:  $V_{\omega} = 70.5 \text{ mm/s}$  and  $f = 2.5 \text{ kHz}$ ,  $Q_s = 2 \mu\text{L/min}$



**Fig. 16** Mixing index at different flow rates; the values shown being those for each individual inlet. Conditions:  $\alpha = 30^\circ$ ,  $V_{\omega} = 70.5 \text{ mm/s}$ , and  $f = 2.5 \text{ kHz}$

be enough to accomplish a homogeneous mixing; however, under larger flow rates (particularly above  $Q_s = 1.5 \mu\text{L/min}$  for the current study), the disturbance brought by a single sharp edge is limited and several additional similar structures should be introduced along the microchannel to achieve good mixing performance.

## 6 Conclusions and perspectives

The main outcome of this study is to investigate the mechanism of AS by direct particle visualization and demonstrate the potentiality for mixing enhancement in microchannels via acoustic streaming around sharp structures. Phenomenologically similar as the Rayleigh streaming, but with strong local Reynolds stress enhancement near the tip, the sharp-edge acoustic streaming is viewed as a promising one, since it enables strong streaming disturbance to the flow with low energy input and low-cost transducers and amplifiers. Indeed, within flat channels, no streaming would be generated at such frequency and amplitude. We use particle visualization and PIV treatment to characterize the AS conditions of appearance, spatial structure, magnitude, and its disturbance level relative to the main stream. The flow characteristics under different experimental conditions (tip angle, vibration amplitude/velocity, and flow rate) are quantitatively investigated.

Our main conclusions are the following.

First, regarding the AS phenomenon, our study confirms the perturbation theory about the boundary layer condition. Sharp edges, whose curvature radius (1.3–5.2  $\mu\text{m}$  in this work) is smaller than the viscous boundary layer (11.3  $\mu\text{m}$  in this work), can achieve strong acoustic streaming flow. Conversely, a round-edge structure with a curvature diameter of 100  $\mu\text{m}$ , is shown to be inefficient for generating acoustic streaming and mixing.

Second, sharper edges and higher vibration amplitude give stronger streaming flows. Under our test conditions, the highest maximum streaming velocity is 75  $\text{mm/s}$  and it is obtained for  $V_{\omega} = 101.7 \text{ mm/s}$  with the sharpest edge angle  $30^\circ$ . Meanwhile, the corresponding vortex can almost cover the whole channel until reaching the opposite channel wall. In terms of shapes of vortices, we observe symmetrical counter-rotating vortices when flow rate is zero, and the upstream/downstream symmetry is broken as the flow rate is turned on. In the latter case, the upstream vortex disappears as  $Q_c$  is set beyond a relatively low value, while the downstream one remains within a larger range of  $Q_c$ . The perturbation distance can also be as large as the channel width under low flow rate and with the sharpest tip, even for moderate vibration magnitude.

Finally, perhaps not implausibly, stronger streaming (with sharper tip and under larger vibration magnitude) helps to achieve better mixing. Significant mixing improvement is witnessed with the fluorescent dye measurement: a mixing index of 0.38 (mostly mixed) when AS is generated, compared to 0.73 when acoustic excitation is off, for the case of  $2 \mu\text{L/min}$ ,  $30^\circ$  tip and under a vibration amplitude of 70.5  $\text{mm/s}$ . In terms of flowrate, mixing enhancement by streaming is obviously weakened at flow

rates above 1.5  $\mu\text{L}/\text{min}$ . In addition, not very intuitively, the disturbance extent is crucial for the mixing application, but not the vortex size itself.

In further studies, the sharp-edge structure could be redesigned in an asymmetrical way, so that the downstream vortices could be restricted while improving the upstream one, the latter being favorable to the mixing efficiency. Another ongoing work is the evaluation of heat transfer (Guo et al. 2014), residence time distribution (Guo et al. 2018), and micromixing performance using chemical iodide–iodate reactions (Guo et al. 2013; Dong et al. 2017). In particular, sharp edges structures are already available in a large number of thermo-fluidic devices, whose performance could potentially benefit from AS generation. Examples include the micropin fins for efficient heat sink design (Chiu et al. 2017; Ambreen and Kim 2018), or ratchet-like microchannel Knudsen pumping thanks to thermal transpiration (Chen et al. 2016; Wang et al. 2019), etc. In summary, AS generated by acoustic fields near sharp structures would also be a heat transfer enhancement that uses both passive and active techniques.

**Acknowledgements** The authors would like to acknowledge the scholarship support from the CSC (China Scholarship Council). Eric Falcon is acknowledged for his help in the measurement of the vibration velocity with the laser vibrometer. They would like to thank the MSC and LIED lab members for their daily support and discussion.

## References

- Ambreen T, Kim M-H (2018) Effect of fin shape on the thermal performance of nanofluid-cooled micro pin-fin heat sinks. *Int J Heat Mass Transf* 126:245–256. <https://doi.org/10.1016/J.IJHEATMASSTRANSFER.2018.05.164>
- Bachman H, Huang P-H, Zhao S et al (2018) Acoustofluidic devices controlled by cell phones. *Lab Chip* 18:433–441. <https://doi.org/10.1039/C7LC01222E>
- Barnkob R, Augustsson P, Laurell T, Bruus H (2012) Acoustic radiation- and streaming-induced microparticle velocities determined by microparticle image velocimetry in an ultrasound symmetry plane. *Phys Rev E Stat Nonlinear Soft Matter Phys* 86:056307. <https://doi.org/10.1103/PhysRevE.86.056307>
- Boluriana S, Morris P (2003) Acoustic streaming: from Rayleigh to today. *Int J Aeroacoustics* 2:255–292. <https://doi.org/10.1260/147547203322986142>
- Bruus H (2012) Acoustofluidics 2: perturbation theory and ultrasound resonance modes. *Lab Chip* 12:20–28. <https://doi.org/10.1039/c1lc20770a>
- Cao Z, Lu C (2016) A microfluidic device with integrated sonication and immunoprecipitation for sensitive epigenetic assays. *Anal Chem* 88:1965–1972. <https://doi.org/10.1021/acs.analchem.5b04707>
- Chen J, Stefanov SK, Baldas L, Colin S (2016) Analysis of flow induced by temperature fields in ratchet-like microchannels by Direct Simulation Monte Carlo. *Int J Heat Mass Transf* 99:672–680. <https://doi.org/10.1016/J.IJHEATMASSTRANSFER.2016.04.023>
- Chiu H-C, Hsieh R-H, Wang K et al (2017) The heat transfer characteristics of liquid cooling heat sink with micro pin fins. *Int Commun Heat Mass Transf* 86:174–180. <https://doi.org/10.1016/J.ICHEATMASSTRANSFER.2017.05.027>
- Dong Z, Zhao S, Zhang Y et al (2017) Mixing and residence time distribution in ultrasonic microreactors. *AIChE J* 63:1404–1418. <https://doi.org/10.1002/aic.15493>
- Eckart C (1948) Vortices and streams caused by sound waves. *Phys Rev* 73:68–76. <https://doi.org/10.1103/PhysRev.73.68>
- Elvira KS, I Solvas XC, Wootton RCR, Demello AJ (2013) The past, present and potential for microfluidic reactor technology in chemical synthesis. *Nat Chem* 5:905–915
- Faraday M (1831) On a peculiar class of acoustical figures; and on certain forms assumed by groups of particles upon vibrating elastic surfaces. *Philos Trans R Soc Lond* 121:299–340. <https://doi.org/10.1098/rstl.1831.0018>
- Franke K, Ross-Messemer M, Menck A et al (2003) The highly sensitive optical measurement of absolute SAW amplitudes for power flow analysis. *IEEE Trans Ultrason Ferroelectr Freq Control* 50:77–80. <https://doi.org/10.1109/TUFFC.2003.1176527>
- Gopinath A, Mills AF (1994) Convective heat transfer due to acoustic streaming across the ends of a Kundt tube. *J Heat Transfer* 116:47–53. <https://doi.org/10.1115/1.2910882>
- Guo X, Fan Y, Luo L (2013) Mixing performance assessment of a multi-channel mini heat exchanger reactor with arborescent distributor and collector. *Chem Eng J* 227:116–127. <https://doi.org/10.1016/j.cej.2012.08.068>
- Guo X, Fan Y, Luo L (2014) Multi-channel heat exchanger-reactor using arborescent distributors: a characterization study of fluid distribution, heat exchange performance and exothermic reaction. *Energy* 69:728–741. <https://doi.org/10.1016/j.energy.2014.03.069>
- Guo X, Fan Y, Luo L (2018) Residence time distribution on flow characterisation of multichannel systems: modelling and experimentation. *Exp Therm Fluid Sci* 99:407–419. <https://doi.org/10.1016/j.expthermflusci.2018.08.016>
- Huang P-H, Xie Y, Ahmed D et al (2013a) An acoustofluidic micro-mixer based on oscillating sidewall sharp-edges. *Lab Chip* 13:3847. <https://doi.org/10.1039/c3lc50568e>
- Huang PH, Xie Y, Ahmed D et al (2013b) An acoustofluidic micro-mixer based on oscillating sidewall sharp-edges. *Lab Chip* 13:3847–3852. <https://doi.org/10.1039/c3lc50568e>
- Huang P-H, Nama N, Mao Z et al (2014) A reliable and programmable acoustofluidic pump powered by oscillating sharp-edge structures. *Lab Chip* 14:4319–4323. <https://doi.org/10.1039/C4LC00806E>
- Huang P-H, Chan CY, Li P et al (2015a) A spatiotemporally controllable chemical gradient generator via acoustically oscillating sharp-edge structures. *Lab Chip* 15:4166–4176. <https://doi.org/10.1039/C5LC00868A>
- Huang PH, Ren L, Nama N et al (2015b) An acoustofluidic sputum liquefier. *Lab Chip* 15:3125–3131. <https://doi.org/10.1039/c5lc0539f>
- Huang P-H, Chan CY, Li P et al (2018a) A sharp-edge-based acoustofluidic chemical signal generator. *Lab Chip* 18:1411–1421. <https://doi.org/10.1039/C8LC00193F>
- Huang PH, Chan CY, Li P et al (2018b) A sharp-edge-based acoustofluidic chemical signal generator. *Lab Chip* 18:1411–1421. <https://doi.org/10.1039/c8lc00193f>
- Lee Dong-Ryul, Loh Byoung-Gook (2007) Smart cooling technology utilizing acoustic streaming. *IEEE Trans Compon Packag Technol* 30:691–699. <https://doi.org/10.1109/tcapt.2007.901756>
- Legay M, Simony B, Boldo P et al (2012) Improvement of heat transfer by means of ultrasound: application to a double-tube heat exchanger. *Ultrason Sonochem* 19:1194–1200. <https://doi.org/10.1016/J.ULTSONCH.2012.04.001>

- Lei J, Glynn-Jones P, Hill M (2013) Acoustic streaming in the transducer plane in ultrasonic particle manipulation devices. *Lab Chip* 13:2133. <https://doi.org/10.1039/c3lc00010a>
- Leibacher I, Hahn P, Dual J (2015) Acoustophoretic cell and particle trapping on microfluidic sharp edges. *Microfluid Nanofluidics* 19:923–933. <https://doi.org/10.1007/s10404-015-1621-1>
- Lighthill SIRJ (1978) ACOUSTIC STREAMING. *J Sound Vib* 61:391–418
- Nama N, Huang P-H, Huang TJ, Costanzo F (2014a) Investigation of acoustic streaming patterns around oscillating sharp edges. *Lab Chip* 14:2824–2836. <https://doi.org/10.1039/C4LC00191E>
- Nama N, Huang PH, Huang TJ, Costanzo F (2014b) Investigation of acoustic streaming patterns around oscillating sharp edges. *Lab Chip* 14:2824–2836. <https://doi.org/10.1039/c4lc00191e>
- Nyborg WL (1953) Acoustic streaming due to attenuated plane waves. *J Acoust Soc Am* 25:68–75. <https://doi.org/10.1121/1.1907010>
- Ovchinnikov M, Zhou J, Yalamanchili S (2014) Acoustic streaming of a sharp edge. *J Acoust Soc Am* 136:22–29. <https://doi.org/10.1121/1.4881919>
- Ozcelik A, Nama N, Huang P-H et al (2016) Acoustofluidic rotational manipulation of cells and organisms using oscillating solid structures. *Small* 12:5120–5125. <https://doi.org/10.1002/sml.201601760>
- Rayleigh JWS (2013) *The theory of sound*, vol One. Dover Publications, New York
- Schneider C, Rasband W, Eliceiri K (2012) ImageJ. *Nat Methods* 9:671–675
- Squires TM, Quake SR (2005) Microfluidics: fluid physics at the nanoliter scale. *Rev Mod Phys* 77:977–1026. <https://doi.org/10.1103/RevModPhys.77.977>
- Stuart JT (1966) Double boundary layers in oscillatory viscous flow. *J Fluid Mech* 24:673. <https://doi.org/10.1017/S0022112066000910>
- Thielicke W, Stamhuis EJ (2014) PIVlab—towards user-friendly, affordable and accurate digital particle image velocimetry in MATLAB. *J Open Res Softw*. <https://doi.org/10.5334/jors.bl>
- Tobias J, Karlsen JT, Bruus H (2015) Forces acting on a small particle in an acoustical field in a thermoviscous fluid Forces acting on a small particle in an acoustical field in a thermoviscous fluid. *Phys Rev E*. <https://doi.org/10.1103/physreve.92.043010>
- Uchida T, Suzuki T, Shiokawa S (1995) Investigation of acoustic streaming excited by surface acoustic waves. In: *IEEE ultrasonics symposium. proceedings. An international symposium. IEEE*, pp 1081–1084
- Wang C, Jalikop SV, Hilgenfeldt S (2012) Efficient manipulation of microparticles in bubble streaming flows. *Biomicrofluidics* 6:012801. <https://doi.org/10.1063/1.3654949>
- Wang X, Zhang Z, Zhang W et al (2019) Numerical simulation of thermal edge flow in ratchet-like periodically patterned microchannels. *Int J Heat Mass Transf* 135:1023–1038. <https://doi.org/10.1016/J.IJHEATMASSTRANSFER.2019.02.006>
- Whitesides GM (2006) The origins and the future of microfluidics. *Nature* 442:368–373. <https://doi.org/10.1038/nature05058>
- Wiklund M, Green R, Ohlin M (2012) Acoustofluidics 14: applications of acoustic streaming in microfluidic devices. *Lab Chip* 12:2438. <https://doi.org/10.1039/c2lc40203c>
- Zacharias J, Ohl C-D (2013) Fluid dynamics, cavitation, and tip-to-tissue interaction of longitudinal and torsional ultrasound modes during phacoemulsification. *J Cataract Refract Surg* 39:611–616. <https://doi.org/10.1016/j.jcrs.2012.10.050>
- Zhao S, He W, Ma Z et al (2019) On-chip stool liquefaction via acoustofluidics. *Lab Chip* 19:941–947. <https://doi.org/10.1039/C8LC01310A>

**Publisher's Note** Springer Nature remains neutral with regard to jurisdictional claims in published maps and institutional affiliations.